OPEN ACCESS

Biomaterials ARTICLE

The Innovation Materials

Microfluidic ultrasmall photothermal AIE nanoparticles for accelerated diabetic wound

Ruihua Dong,[1,2,5] Fulong Ma,[1,3,5] Zijuan Meng,[1,5] Xiaohua Ji,[2,5] Haifei Wen,[1] Haoran Wang,[1] Rui Zhu,[4,*] Zheng Zhao,[1,*] and BenZhong Tang[1,*]

*Correspondence: zhurui_0330@ahmu.edu.cn (R.Z.); zhaozheng@cuhk.edu.cn (Z.Z.); tangbenz@cuhk.edu.cn (B.T.)

Received: December 3, 2025; Accepted: April 23, 2026; Published Online: April 23, 2026; https://doi.org/10.59717/j.xinn-mater.2026.100216

GRAPHICAL ABSTRACT

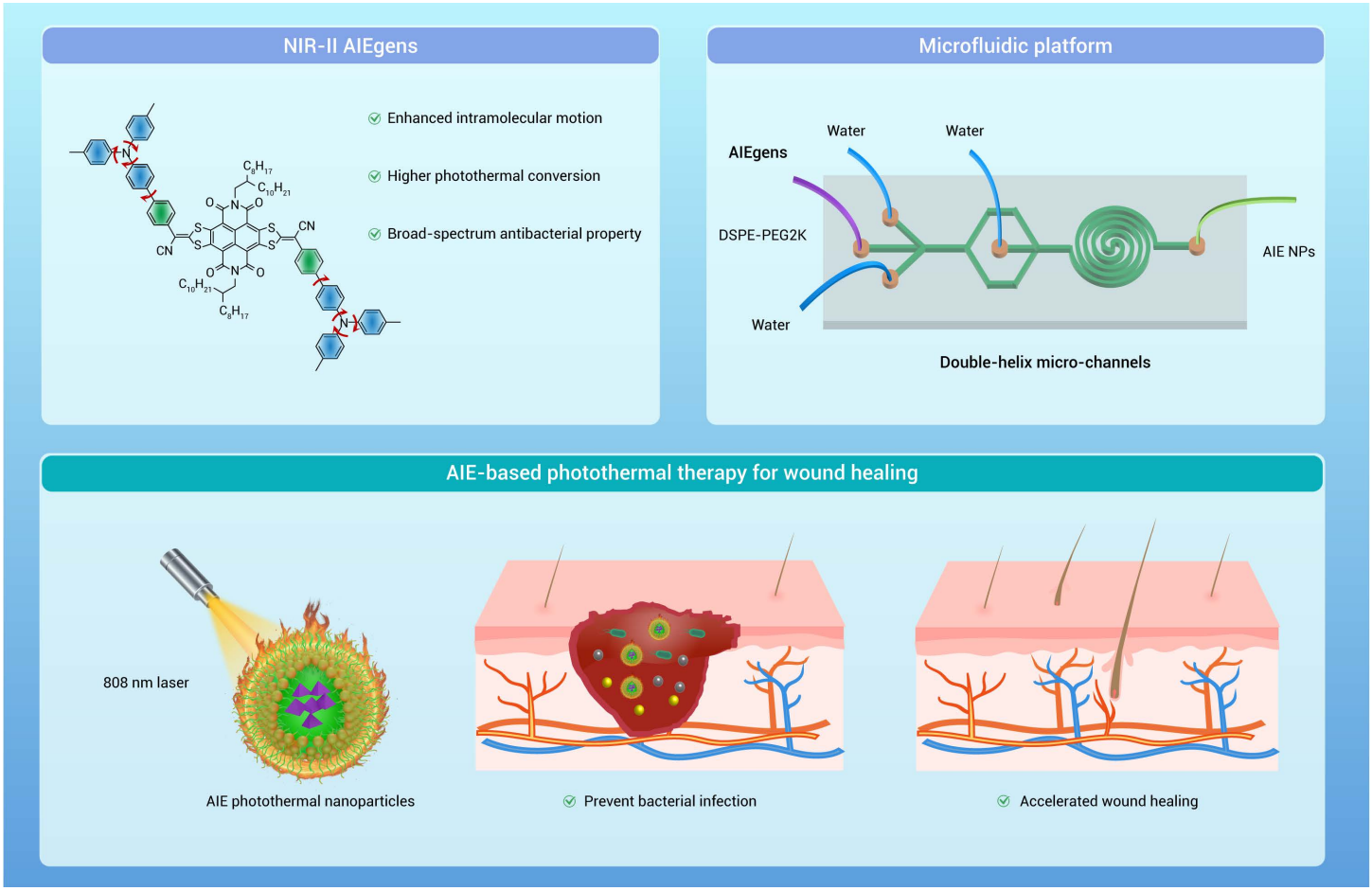

PUBLIC SUMMARY

- This study develops an NIR-II AIEgen with high photothermal efficiency for wound care.
- Microfluidics enables ultrasmall AIE nanoparticles with antibacterial activity and biocompatibility.
- AIE photothermal nanoparticles prevent bacterial infections and accelerate chronic wound healing.

ARTICLE Biomaterials

OPEN ACCESS

Microfluidic ultrasmall photothermal AIE nanoparticles for accelerated diabetic wound

Ruihua Dong,[1,2,5] Fulong Ma,[1,3,5] Zijuan Meng,[1,5] Xiaohua Ji,[2,5] Haifei Wen,[1] Haoran Wang,[1] Rui Zhu,[4,*] Zheng Zhao,[1,*] and BenZhong Tang[1,*]

[1]Guangdong Basic Research Center of Excellence for Aggregate Science, School of Science and Engineering, The Chinese University of Hong Kong (Shenzhen), Shenzhen 518172, China

[2]Qingdao Center of Technology Innovation for AIE Theranostics and Rehabilitation, School of Rehabilitation Sciences and Engineering, University of Health and Rehabilitation Sciences, Qingdao 266113, China

[3]College of Chemistry, Chemical Engineering and Materials Science, Soochow University, Suzhou 215123, China

[4]Department of Nursing, The First Affiliated Hospital of Anhui Medical University, Hefei 230022, China

[5]These authors contributed equally

*Correspondence: zhurui_0330@ahmu.edu.cn (R.Z.); zhaozheng@cuhk.edu.cn (Z.Z.); tangbenz@cuhk.edu.cn (B.T.)

Received: December 3, 2025; Accepted: April 23, 2026; Published Online: April 23, 2026; https://doi.org/10.59717/j.xinn-mater.2026.100216

Citation: Dong R., Ma F., Meng Z., et al. (2026). Microfluidic ultrasmall photothermal AIE nanoparticles for accelerated diabetic wound. *The Innovation Materials* **4**:100216.

Therapeutic strategies are critical for the effective management of diabetic wounds, which are often complicated by persistent infections and slow healing. Conventional wound dressings offer limited therapeutic efficacy and adaptability across diverse clinical scenarios. Here, we report the development of near-infrared II (NIR-II) photothermal nanoparticles based on aggregation-induced emission luminogens (AIEgens) to address these challenges. Benefiting from unrestricted intramolecular motion in the aggregated state, AIEgens demonstrate high photothermal conversion efficiency under 808 nm irradiation. Integration with a microfluidic synthesis platform enables precise control over nanoparticle size, resulting in ultrasmall AIE nanoparticles (~ 20 nm) with excellent biocompatibility and broad-spectrum antibacterial activity. Upon in situ deposition onto infected wounds, these AIE nanoparticles function as efficient photothermal agents, providing adaptable and comfortable coverage while markedly accelerating diabetic wound healing. This work not only introduces a versatile photothermal platform for infection-responsive therapy but also offers a promising strategy for the development of AIE-based healthcare.

INTRODUCTION

Diabetes mellitus has become a major global health burden, affecting 10.5% of adults aged 20-79 years and ranking among the leading causes of morbidity and mortality.[1-3] Among its severe complications, chronic diabetic wounds pose a persistent clinical challenge due to delayed healing, often requiring 8-12 weeks to close. These wounds are further complicated by sustained hyperglycemia, which exacerbates inflammation, promotes bacterial colonization, particularly by multidrug-resistant (MDR) strains, and impairs tissue regeneration.[4-6] As a result, diabetic wounds may stall at any phase of the healing process, including inflammation, proliferation, and remodeling, increasing the risk of recurrent bacterial infections and mortality.[7,8] Current clinical treatments, such as antibiotic therapy and wound dressings, often fail to address these challenges effectively.[9,10] This highlights the urgent need for advanced therapies capable of both combating MDR bacterial infections and facilitating tissue repair throughout the protracted healing process.[11-13]

Photothermal therapy (PTT) has emerged as a promising strategy for antibacterial treatment and wound healing.[14-16] By converting near-infrared (NIR) light into localized heat, PTT enables precise bacterial eradication with minimal damage to surrounding tissues.[17,18] Compared to traditional antibacterial approaches, PTT offers high spatial-temporal selectivity, non-invasiveness, and favorable biocompatibility.[19,20] However, achieving high photothermal conversion efficiency (PCE) under low-power irradiation remains a key challenge.[21,22] Clinically approved organic photothermal agents, such as indocyanine green (ICG) and methylene blue (MB), have demonstrated clinical safety and biodegradability.[23,24] Nonetheless, conventional organic molecules suffer from π−π stacking, which limits the boost of photothermal efficiency in the aggregate state, ultimately limiting their biomedical utility.[25-27]

Aggregation-induced emission (AIE) materials provide a viable alternative to the limitations of conventional organic photothermal agents.[28-30] Unlike traditional organic molecules that suffer from aggregation-caused quenching (ACQ), the highly distorted molecular skeleton of AIE materials provides ample space for its active molecular motion, which leads to superior photothermal conversion efficiency in the aggregate state.[31-33] These properties make them ideal candidates for biomedical applications, including antibacterial phototherapy and real-time imaging.[34-36] Despite their advantages, AIE-based photothermal agents can exhibit challenges such as hydrophobicity and uncontrolled nanoparticle aggregation, which limit their bioavailability and therapeutic efficacy.[37,38] Addressing these issues requires rational AIE nanoparticle engineering to achieve optimized physicochemical properties and enhanced therapeutic outcomes.

To enhance the therapeutic performance of AIE-based PTT agents, this study develops near-infrared II (NIR-II) AIE-based photothermal nanoparticles fabricated via a microfluidic platform for diabetic wound treatment (Scheme 1). The designed nanoparticles exhibit strong absorption in the NIR-II region, ensuring deep tissue penetration and efficient heat generation for the eradication of bacteria and wound healing. A dual-spiral microfluidic chip was used to precisely control nanoparticle size, resulting in uniform particles ranging from 20 to 200 nm. Surface modification with polyethylene glycol (PEG) further improved the nanoparticles' stability and biocompatibility, facilitating prolonged circulation and targeted accumulation at the wound site, and demonstrating significant potential for accelerated chronic wound management.

MATERIALS AND METHODS

Materials and reagents

All chemical reagents used were commercially purchased and were used without further processing. Organic reagents such as tetrahydrofuran (THF), anhydrous ethanol, and N,N-Dimethylformamide (DMF) were purchased from Sinopharm Chemical Reagent Co., Ltd. DSPE-mPEG2k was obtained from Avanti, USA. Staphylococcus aureus (ATCC 6538P), Escherichia coli (ATCC 25922), and other strains of antibiotic-resistant bacteria were all sourced from the China General Microbiological Culture Collection Center. DMEM medium, fetal bovine serum, and penicillin/streptomycin were purchased from Gibco, USA. The pure water used in the experiments was ultrapure water filtered through a Millipore water system.

Fabrication of microfluidic chips

As shown in Figure S1, the microfluidic chip consists of 3 inlets, 1 outlet, 1 straight mixing channel, and 1 double helical mixing channel. The double helix channel is divided into 3 positive helical loops and 3 reverse helical loops, connected through an S-shaped channel. The width of the inlet channels is 100 μm, while other channels have a width of 300 μm, and a height of 60 μm. The microfluidic chip is fabricated using a glass substrate and a polydimethylsiloxane (PDMS) slab. Four plastic tubes are connected to the three inlets and one outlet, with three needles inserted at the ends of the inlet tubes. The microchannel pattern is transferred onto the PDMS slab from a photomask using standard soft-lithography techniques.

Preparation of AIE nanoparticles

As illustrated in Scheme 1, photothermal molecules with solid-state molecular motion and high-efficiency non-radiative transitions were synthesized in two steps, and theoretical calculations were carried out on the

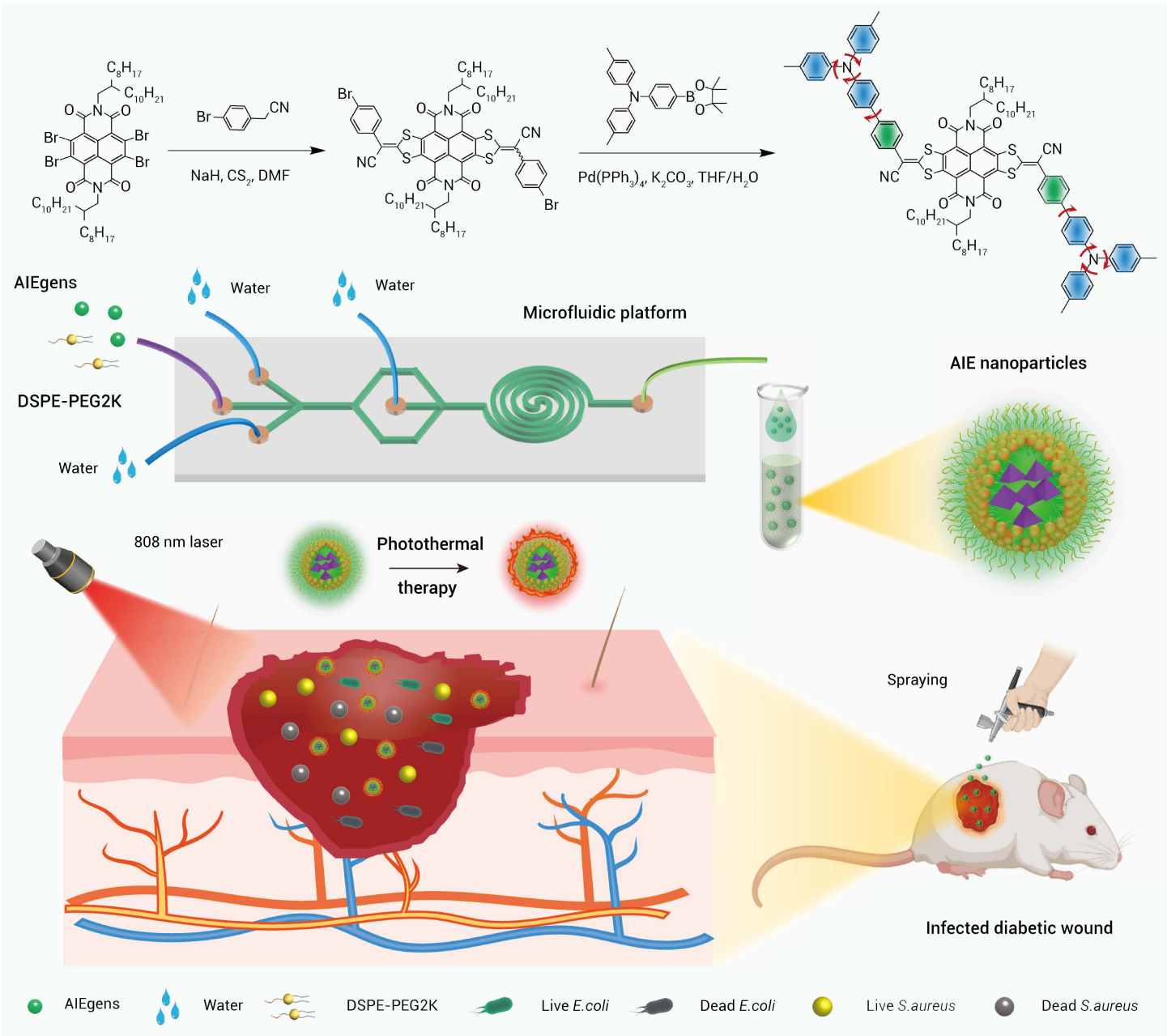

Scheme 1. Schematics of microfluidic photothermal AIE nanoparticles for accelerated healthcare of diabetic wound healing NIR-II AIE molecule (namely NDA-MePA) was synthesized through two reaction steps and fabricated into nanoparticles using a microfluidic chip.

molecular structure. After completing the synthesis of photothermal molecules, the microfluidic chip platform was used to assemble and encapsulate the molecules to prepare water-soluble photothermal nanoparticles. During the synthesis process on the microfluidic platform, 2 mg of the synthesized photothermal molecule and 8 mg of DSPE-mPEG2k were dissolved in 2 mL of THF to prepare a solution with a concentration of 1 mg/mL. This mixed solution was injected into the inlet of the microfluidic chip through a syringe pump at a flow rate of 3 mL/h. Ultrapure water was introduced from the side inlets of the microfluidic chip at a rate of 120 mL/h. After thorough mixing in the double helix channel of the microfluidic chip, PEG-coated water-soluble photothermal nanoparticles can be collected at the outlet. The preliminary nanoparticle solution contained residual THF solvent, which required rotary evaporation and ultrafiltration centrifugation to obtain the final nanoparticle aqueous solution.

Characterization of AIE nanoparticles

After the nanoparticles synthesized by the microfluidic chip were processed through rotary evaporation and ultrafiltration, their particle size was analyzed using DLS (Zetasizer 3000HS), especially to test the effect of different ultrapure water injection rates on the size of the nanoparticles. The prepared nanoparticles were then drop-cast onto copper grids coated with an ultra-thin carbon film and dried overnight at room temperature. Their surface morphology was characterized using TEM.

Biocompatibility of AIE nanoparticles

Subsequently, the nanoparticle solution, post rotary evaporation and ultrafiltration, was formulated into different concentrations (10 μg/mL, 20 μg/mL, and 40 μg/mL) to validate the cellular compatibility of the nanoparticles through a cell viability assay. HUVEC and 3T3 cells were pre-cultured in confocal dishes, with a seeding density of 5×10^4. They were co-incubated with nanoparticles at different particle concentrations and placed in a 37°C cell incubator with 5% CO_2 overnight. After that, the culture medium was removed, and cell live/dead dye (DAPI/PI) was added. The effect of nanoparticles on cell viability was observed under a laser confocal microscope. Furthermore, nanoparticles with a concentration of 40 μg/mL were injected into BALB/c mice via tail vein. After a month, tissue sections of major organs

(heart, liver, spleen, lungs, and kidneys) were observed to evaluate the biosafety of the nanoparticles.

Evaluation of photothermal efficiency

The photothermal performance of the nanoparticles was systematically evaluated using an infrared thermal imaging camera (FLIR Systems, USA) under varying laser power densities and irradiation distances. Temperature elevation profiles were recorded for nanoparticle dispersions at concentrations of 10, 20, and 40 μg/mL to quantitatively assess their photothermal conversion efficiency. To investigate antibacterial efficacy, multidrug-resistant Escherichia coli (*MDR E.coli*) and methicillin-resistant Staphylococcus aureus (*MRSA*) were employed as representative bacterial models. Bacterial suspensions were incubated with different concentrations of nanoparticles for 20 minutes, followed by laser irradiation (0.5 W/cm^2, 13 cm distance) for 10 minutes. Bactericidal effects were evaluated via colony-forming unit (CFU) assays, bacterial viability staining, crystal violet (CV) staining test and confocal laser scanning microscopy with 3D biofilm reconstruction.

Evaluation of photothermal therapy

For *in vivo* assessment, diabetic BALB/c mice (female, 25 g) were preconditioned with streptozotocin (30 mg/mL) administered seven days prior to model establishment. Full-thickness infected wound models were created on the dorsal surface by inoculating MDR bacteria at a concentration of 1×10^7 CFU. AIE-based photothermal nanoparticles (40 μg/mL, 100 μL) were applied topically to the infected wound sites, followed by a 20-minute incubation and subsequent NIR laser irradiation (0.5 W/cm^2, 13 cm) for 10 minutes. Wound healing progression and therapeutic efficacy were monitored on days 3, 5, 10, and 15 post-treatment.

Statistical analysis was performed using GraphPad Prism (version 10.1.2) and Origin (version 2021). All data are presented as the mean ± standard deviation (SD). Comparisons between groups were conducted using two-way ANOVAs. A P value < 0.05 was considered statistically significant. Statistical significance is denoted as follows: $*p < 0.05$, $**p < 0.01$, $***p < 0.001$.

RESULTS

Molecular design and synthesis of NIR-II AIEgen

As illustrated in Scheme 1, the naphthalene diimide-fused 2-(1,3-dithiol-2-ylidene)acetonitrile (NDA) moiety with extensive π-conjugation was utilized as an acceptor. 4-methyl-N-phenyl-N-(p-tolyl)aniline, serving as both a donor and a rotor featuring freely rotatable benzene rings, was directly coupled to the NDA moiety to afford NDA-MePA. Meanwhile, long alkyl chains positioned on the side of the conjugated molecular backbone were employed to weaken intermolecular interactions, thereby providing ample space for excited-state rotor motion. Such a structural arrangement will facilitate efficient radiative transition processes and enhance photothermal performance. Simultaneously, strong intramolecular donor–acceptor (D-A) interactions were anticipated to narrow the energy gap, leading to a red-shifted absorption band that aligns with the commercial 808 nm laser. The chemical structure of NDA-MePA was verified by ^{1}H NMR, ^{13}C NMR, and high-resolution MALDI-TOF mass spectrometry, yielding satisfactory results (see Figures S2-S3). The molecular structure and purity of the synthesized AIE molecules were confirmed by spectroscopic analysis, which revealed well-resolved characteristic peaks consistent with the proposed chemical structures, indicating successful synthesis without detectable impurities.

Photophysical properties and theoretical calculation

To further investigate the photophysical properties and electronic interactions at the molecular level, theoretical calculations using the Gaussian 09 program were performed. As shown in Figures 1A-C, due to its electron-deficient nature, the lowest unoccupied molecular orbital (LUMO) electron cloud of the NDA-MePA molecule is primarily distributed over the NDA acceptor moiety, while the highest occupied molecular orbital (HOMO) electron cloud is mainly located on the electron-donating fragment. This separated HOMO–LUMO distribution indicates that NDA-MePA exhibits intramolecular charge transfer (ICT) transition characteristics, resulting in a small molecular energy gap (1.26 eV). The torsion angles between the molecular fragments are 33.2° and 41°, respectively, which helps to suppress intermolecular π-π interactions and facilitate the motion of the molecular excited state.

To analyze their absorption and emission characteristics, UV-visible-near-infrared (UV-NIR) and photoluminescence (PL) spectra were measured. The optical properties of the NDA-MePA molecule were investigated in DMF/H_2O mixtures. As shown in Figures 1D-E, the NDA-MePA molecule exhibited a maximum absorption wavelength at 725 nm and a maximum emission at 1055 nm. NDA-MePA molecule showed elongated emission wavelengths with a portion of the emission spectrum in the NIR-II window. Then, the AIE feature of the NDA-MePA molecule was analyzed by monitoring its fluorescence in a DMF/H_2O mixed solvent with varying water fractions. Figures 1F & S4 illustrate that the NIR-II molecule manifested weak fluorescence in pure DMF, with its fluorescence gradually intensifying as the water fraction increased, signifying its favorable performance of AIE.

Fabrication and characterization of AIE nanoparticles

After the synthesis of the photothermal molecule was completed, the molecular surface was PEG-coated using a microfluidic chip (Figures 1G & S4). At different feed flow rates (30 mL/h-120 mL/h), the size of the water-soluble nanoparticles obtained was significantly different. At the highest flow rate of 120 mL/h, the nanoparticles measured approximately 18 nm in diameter. As the pure water feed flow rate decreased, the size of the nanoparticles gradually increased, with the largest size being around 200 nm (Figure 1H). Ultra-small nanoparticles prepared at a flow rate of 120 mL/h were observed using a transmission electron microscope, revealing that the sizes of the nanoparticles were relatively uniform, mostly dispersed within the 10-20 nm range (Figure 1I).

Next, the biocompatibility of microfluidic nanoparticles at different concentrations was evaluated using cell experiments and animal experiments. Firstly, the nanoparticles synthesized by microfluidics were subjected to rotary evaporation and ultrafiltration to remove the THF solvent and DSPE-mPEG2k residues from the solution, resulting in aqueous solutions with concentrations of 10 μg/mL, 20 μg/mL, and 40 μg/mL. HUVEC cells and NIH-3T3 cells were chosen as experimental cell lines. They were pre-planted on the surface of confocal dishes, and then incubated with nanoparticles of different concentrations. Observations were made using live/dead cell staining and a laser scanning confocal microscope. As shown in Figure 1J, after incubation with nanoparticles of different concentrations, both HUVEC and 3T3 cells exhibited high viability. Even at the highest concentration of 40 μg/mL, cell growth was not significantly affected, thus proving the excellent cytocompatibility of the nanoparticles. Furthermore, using the cell counting kit-8 (CCK-8) assay kit, the effect of nanoparticles on cell proliferation was quantitatively evaluated. As seen in Figures 1K & S5 , cell proliferation did not show significant changes with increasing nanoparticle concentrations. Flow cytometry analysis revealed only a slight increase in fluorescence intensity in mammalian cells after 30 min incubation with AIE nanoparticles, even at higher concentrations, indicating minimal cellular internalization (Figure S6). Consistently, live/dead staining under NIR irradiation showed that L929 cells treated with AIE nanoparticles (40 μg/mL) maintained high viability, comparable to the untreated control group. To further evaluate biocompatibility, metabolism studies under local wound treatment conditions suggested that the nanoparticles were primarily cleared through the wound skin rather than systemic circulation (Figure S7). Finally, through tail vein injection and tissue sectioning, the results also confirmed the tissue compatibility of the microfluidic photothermal nanoparticles, showing no impact on major organs such as the heart, liver, spleen, lungs, and kidneys (Figure S8). Moreover, 1-month *in vivo* studies following either local wound administration or intravenous injection revealed no observable pathological damage in major organs, demonstrating favorable long-term biosafety (Figure S9). In summary, the water-soluble photothermal nanoparticles prepared using the microfluidic chip have the advantage of controllable size, with the smallest nanoparticles measuring around 20 nm in diameter, and the microfluidic nanoparticles demonstrate excellent cellular and tissue compatibility.

Antibacterial activity of AIE nanoparticles

To explore the antibacterial property of AIE nanoparticles, the photothermal generation efficiencies were firstly investigated under the irradiation of 808 nm laser at the concentration of 0-40 μg/mL. A laser power density of

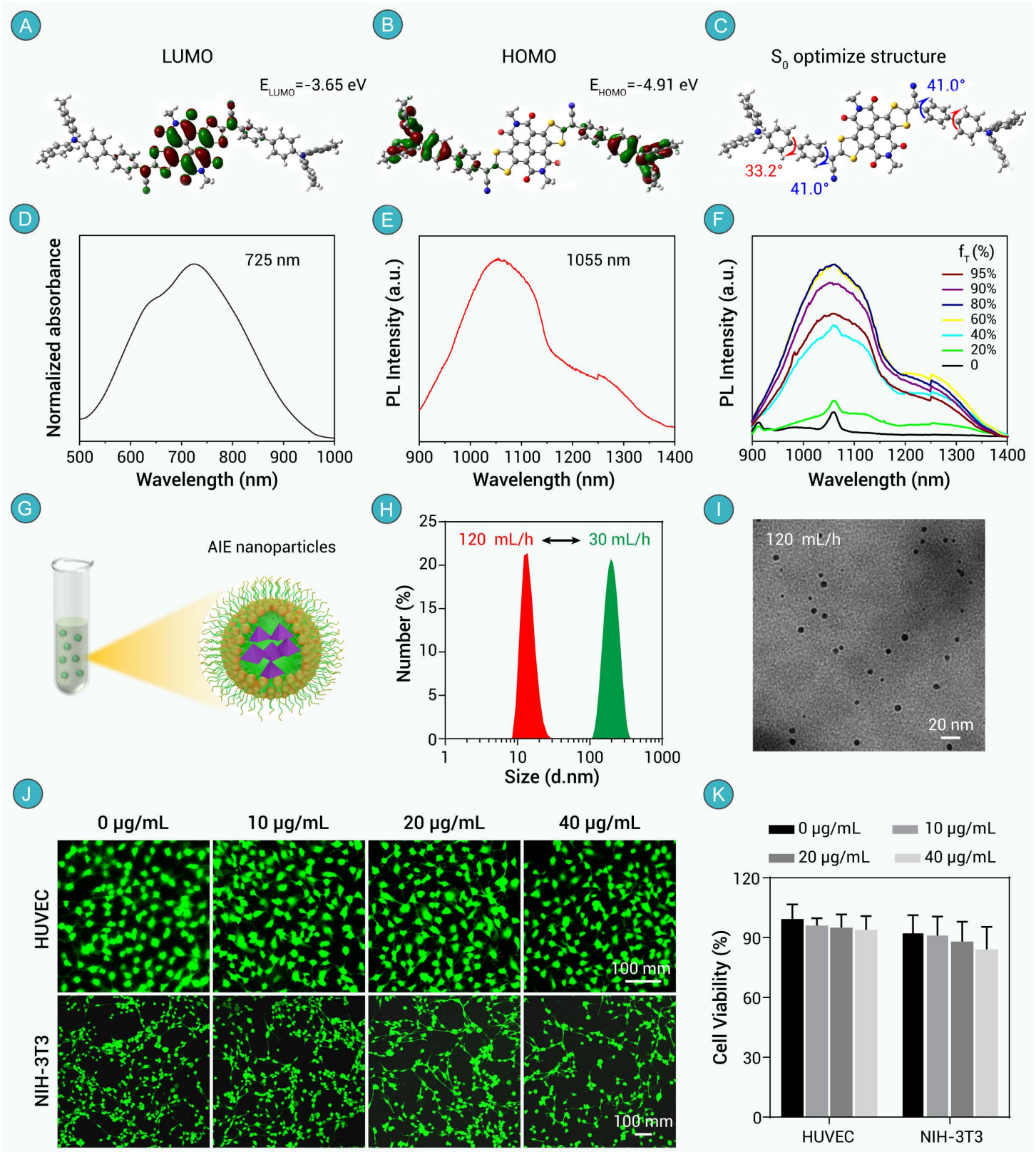

Figure 1. Photophysical properties and cell viability of AIE nanoparticles (A) Theoretical calculation of the LUMO of the photothermal molecule. (B) Theoretical calculation results of the HOMO of the photothermal molecule. (C) Calculation of the torsion angle of the photothermal molecule. (D) The absorption spectra of NDA-MePA in DMF/H_2O mixtures. (E) The PL spectra of NDA-MePA in DMF/H_2O mixtures. (F) PL spectra of NDA-MePA in DMF/H_2O mixtures with different toluene fractions (f_T). (G) Schematic of the microfluidic nanoparticle encapsulation. (H) Particle size distribution results of the microfluidic nanoparticles. (I) TEM image of ultra-small nanoparticles. (J) Live/dead staining results of cells after incubation with nanoparticles of different concentrations on HUVEC cells and 3T3 cells. (K) Cell viability statistics after treatment with nanoparticles.

0.5 W/cm^2 and an irradiation height of 13 cm were chosen to test the heat production of the nanoparticles. From Figures 2A-B, it can be observed that as the concentration of AIE nanoparticles increases, the generated temperature also rises, reaching a maximum of 55°C within 5 minutes, which fully meets the temperature requirements for photothermal therapy. The temperature change of AIE nanoparticles solution (40 μg/mL) under 808 nm irradia-

tion at 0.5 W/cm^2 was confirmed for effective photothermal therapy (43°C) to eliminate bacteria *in vivo*.[39] As displayed in Figure 2C, the photothermal stability of AIE nanoparticles (40 μg/mL) was evaluated by 4 "ON/OFF" cycles of laser irradiation, which further confirmed the heating and cooling capacity. The AIE nanoparticles exhibited a photothermal conversion efficiency (PCE) of 32.4%. While not the highest among reported photothermal systems, this efficiency is adequate to achieve rapid and effective antibacterial performance (Figure S10). AIE nanoparticles retained superior photothermal stability, displaying ideal advantages for long-term antibacterial treatment. Meanwhile, the microfluidic AIE nanoparticles also demonstrated excellent NIR-II imaging and photothermal performance. Using a mouse subcutaneous tumor model, the *in vivo* biodistribution and photothermal behavior of the AIE nanoparticles were monitored *in situ*. As shown in Figures S11-S14, the AIE nanoparticles exhibited outstanding NIR-II imaging and photothermal capabilities. Moreover, the stability of the AIE nanoparticles was significantly enhanced by PEGylation. As shown in Figure S15, the PEGylated AIE nanoparticles exhibited good colloidal stability in H_2O, PBS, and FBS. No obvious metabolic distribution or accumulation of the nanoparticles in the blood or major organs was observed during the local wound treatment period (Figure S16). In addition, blood circulation studies indicated that the nanoparticles exhibited an extended *in vivo* half-life of more than 4 h (Figure S17).

Inspired by the ideal photothermal conversion efficiency of AIE nanoparticles, we carried out *in vitro* photothermal antibacterial performance of AIE nanoparticles. Considering that chronic wounds often suffer from MDR bacterial infections during the delayed healing process, MDR *Staphylococcus aureus* (MRSA) and *Escherichia coli* (MDR *E.coli*) were used as Gram-positive and Gram-negative bacterial models. A standard plant counting approach was used for evaluating the antibacterial activity of AIE nanoparticles. AIE nanoparticles of different concentrations were incubated with two antibiotic-resistant bacteria to test the photothermal sterilization performance. Within the tested concentration range, AIE NPs exerted no appreciable effect on bacterial viability in the absence of laser irradiation, indicating minimal dark toxicity (Figure S18). By contrast, as shown in Figure 2D, under the laser irradiation, as the NPs concentration increased, the magnitude of the temperature rise was amplified, which in turn further suppressed bacterial viability and concomitantly enhanced bactericidal efficacy. Ultimately, at a concentration of 40 μg/mL, a 10-minute laser irradiation was sufficient to completely eradicate both MRSA and MDR *E.coli*, demonstrating excellent photothermal sterilization effects and spectral sterilization capabilities (Figure 2E). Lastly, we utilized the confocal microscope to investigate the photothermal antibacterial properties of AIE nanoparticles. Syto9 and propidium iodide (PI) were used to present the live/dead bacterial activity after PTT treatment with AIE nanoparticles. As shown in Figure 2F, fluorescence confocal images confirmed the effective eradication of two MDR bacteria. With increasing the concentration of AIE nanoparticles, more red/dead bacteria were observed, demonstrating the excellent antibacterial activity of AIE nanoparticles for preventing bacterial infections. In addition, the antibiofilm activity of AIE NPs was quantified using a crystal violet (CV) assay, with CV absorbance serving as a surrogate for total biofilm biomass. For MRSA, compared with non-irradiated controls, 808 nm laser activation induced a concentration-dependent decrease in CV absorbance, indicating a marked reduction in biofilm accrual and demonstrating a light-triggered antibiofilm effect (Figures S19-S20). As morphological corroboration, confocal laser scanning microscopy with 3D reconstruction revealed concomitant decreases in biofilm thickness, reduced surface coverage, and disrupted matrix continuity, consistent with the CV readouts (Figure S21). Collectively, these findings substantiate the nanoparticle's potent antibacterial performance and its efficacy in suppressing biofilm formation under photonic activation. antibiofilm-related experiments demonstrated that the nanoparticles not only effectively inhibited biofilm formation but also disrupted established biofilms under NIR laser irradiation, highlighting their relevance for treating biofilm-associated bacterial infections. To clarify the antibacterial mechanism, reactive oxygen species (ROS) generation was evaluated using the DCFH-DA probe. The nanoparticles exhibited only ~ 4-fold higher ROS levels than the water control, indicating negligible photodynamic activity and excluding ROS-mediated antibacterial effects. In contrast, upon 808 nm laser irradiation, the pronounced photothermal heating disrupted bacterial membranes and biofilm structures, thereby inhibiting biofilm formation and effectively eradicating pre-formed biofilms (Figure S22).

In situ deposited AIE nanoparticles for wound care

In vitro antibacterial tests demonstrated the excellent cell compatibility, photothermal conversion performance, and photothermal sterilization capability of the microfluidic nanoparticles. The optimal antibacterial concentration was determined to be 40 μg/mL, with a laser power of 0.5 W/cm^2, an irradiation height of 13 cm, and an irradiation duration of 10 min. Subsequently, an in-depth evaluation of the photothermal sterilization performance of the nanoparticles was carried out using animal experiments. As shown in Figure 3A, female BALB/c mice were pre-injected with streptozotocin to induce diabetes symptoms. Skin wounds were created on the backs of the mice, followed by bacterial infection using antibiotic-resistant strains. The wounds were then sprayed with photothermal AIE nanoparticles for photothermal antibacterial treatment, and changes in wound area throughout the healing process were observed. From Figure 3B, within a 15-day treatment period, the healing speed of the diabetic wounds treated with nanoparticle photothermal therapy significantly accelerated. In contrast, wounds in the control group experienced severe bacterial infections and purulent symptoms, resembling the condition of clinical diabetic wounds. From the statistics on wound area (Figures 3C-D), it's evident that for infectious wounds caused by both antibiotic-resistant gram-negative and gram-positive bacteria, AIE nanoparticles photothermal treatment significantly enhances the wound healing speed and repair conditions. Throughout the animal treatment process, a thermal imager was used to continuously record the laser irradiation conditions on the wounds. As Figures 3E-F show, AIE nanoparticles sprayed on the surface of mouse wounds can achieve temperatures as high as 53°C, effectively killing antibiotic-resistant bacteria on the wound surface. In summary, based on microfluidic nanoparticles, photothermal sterilization treatment can be applied to infected diabetic wounds, significantly accelerating the healing process of diabetic wounds.

Photothermal AIE nanoparticles for diabetic wound healing

Furthermore, to verify the therapeutic effect of photothermal nanoparticles on infectious wounds, we employed Western blot experiments to quantitatively analyze the tissue of infected wounds five days after treatment. As can be seen from Figure 4A, compared to the control group, the photothermal nanoparticle treatment group exhibited a significantly lower level of immune expression. Statistical results indicate that the amounts of two inflammatory cytokines, IL-6 and TNF-α, were notably reduced in wound tissues after photothermal treatment, suggesting a significant improvement in the infection status of the wound (Figures 4B-C). This further substantiates the antibacterial effect of photothermal treatment. More in-depth immunofluorescence images also confirm the antibacterial effect of nanoparticle photothermal treatment, which can significantly inhibit wound infection. The immunofluorescence images of CD31, CD86, CD206, and F4-80 factors in the surrounding wound tissue clearly indicate the inflammatory condition of the wound tissue after treatment (Figure 4D). On the 10th day of wound treatment, surrounding tissues were excised, ground, and bacterial plated. From Figures 4E-F, compared to the control group, bacterial infection in the wound was significantly improved after photothermal treatment with nanoparticles. The inflammatory response in the tissue was notably suppressed, facilitating rapid healing of chronic diabetic wounds.

Finally, through immunohistochemical HE staining and Masson staining, the treated wound tissues were observed to evaluate the wound healing and repair effects. As shown in Figures 5A-B, the wound tissue regeneration level in the nanoparticle photothermal treatment group was higher, and the degree of epithelial regeneration was significantly greater than that in the control group. Furthermore, the collagen deposition in the wound tissue of the photothermal treatment group was notably higher than in the standard control group, indicating a marked enhancement in wound healing and regeneration levels (Figure 5C). Throughout the wound healing process, by continuously monitoring the weight of diabetic mice, results also showed that photothermal treatment is safe, as there was no significant weight change compared to the control group (Figure 5D). Hemolysis experiments were used to quantitatively evaluate the blood compatibility of the nanoparticles.

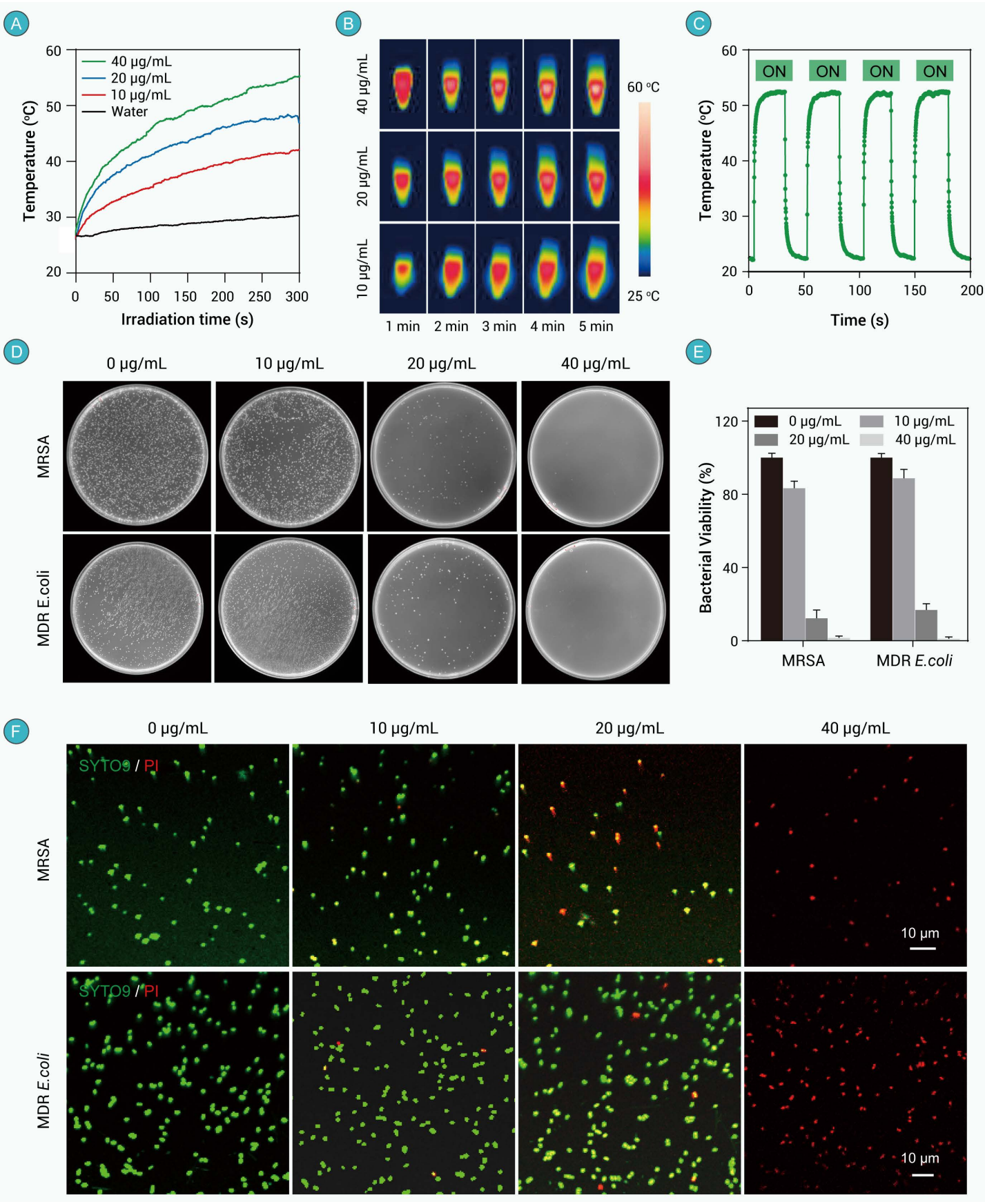

Figure 2. Photothermal properties and antibacterial activity of AIE nanoparticles (A) Temperature change curve of nanoparticle solutions of different concentrations after irradiation with an 808 nm laser. (B) Infrared imaging of nanoparticles of different concentrations after irradiation with an 808 nm laser. (C) Photothermal stability of AIE nanoparticles (40 μg/mL) during 4 on/off irradiation cycles under 808 nm laser at 0.5 W/cm^2. (D) Bacterial plating results after photothermal sterilization of nanoparticles at different concentrations. (E) Bacteria survival rate of MRSA and MDR *E.coli* treated with AIE nanoparticles (40 μg/mL). (F) Confocal images of live/dead staining of bacteria after photothermal treatment. Live (Syto 9, green) and dead (PI, red).

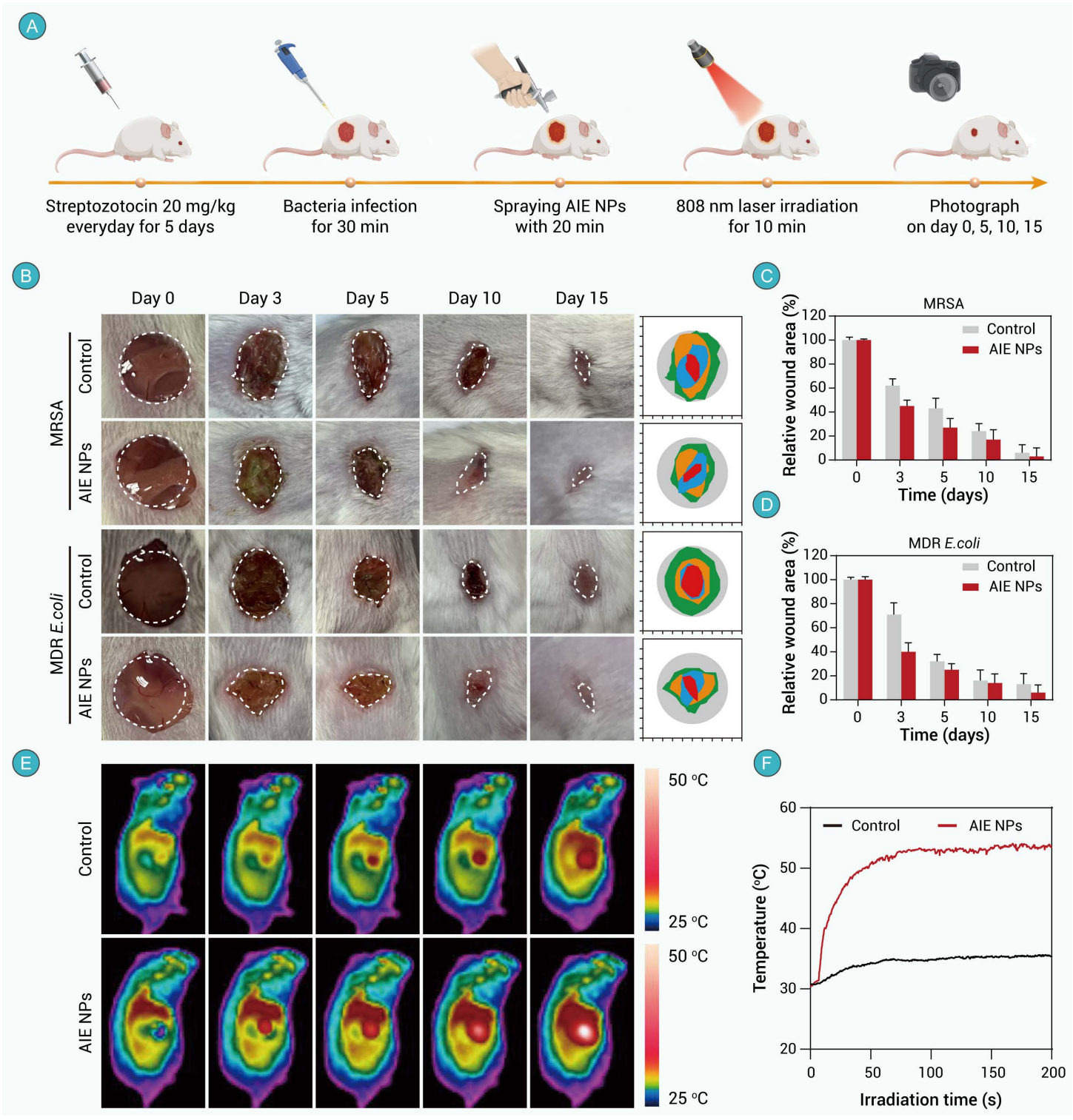

Figure 3. AIE photothermal nanoparticles for diabetic wound healing (A) Construction and treatment process of diabetic wounds. (B) Comprehensive recording of wound healing progress throughout the healing process. (C) Area statistics for infectious wounds caused by antibiotic-resistant Staphylococcus aureus (data presented mean ± SD, n=6). (D) Area statistics for infectious wounds caused by antibiotic-resistant *E.coli* (data presented mean ± SD, n=6). (E) Thermal imaging recordings of the wound surface during the photothermal treatment process. (F) Temperature change statistics of the wound surface after laser irradiation.

The results revealed that the red blood cell compatibility of the nanoparticles meets the requirements for *in vivo* animal experiments (Figure 5E). In conclusion, the animal experimental model successfully demonstrated that nanoparticle photothermal treatment can effectively inhibit bacterial infections in diabetic wounds, accelerate tissue repair and skin regeneration, and greatly promote wound healing outcomes.

Many conventional photothermal agents suffer from aggregation-caused quenching (ACQ) or compromised photothermal performance in the aggregated state, which limits their practical biomedical applications. In this work, NDA-MePA is an aggregation-induced emission (AIE)-active photothermal molecule, whose photophysical properties are particularly advantageous under aggregated or nanoparticle-confined conditions. NDA-MePA can maintain highly efficient intramolecular motion in the solid and aggregated states within nanoparticles, which promotes non-radiative decay pathways. Most of the absorbed optical energy is dissipated as heat, leading to enhanced photothermal conversion efficiency, while simultaneously providing strong

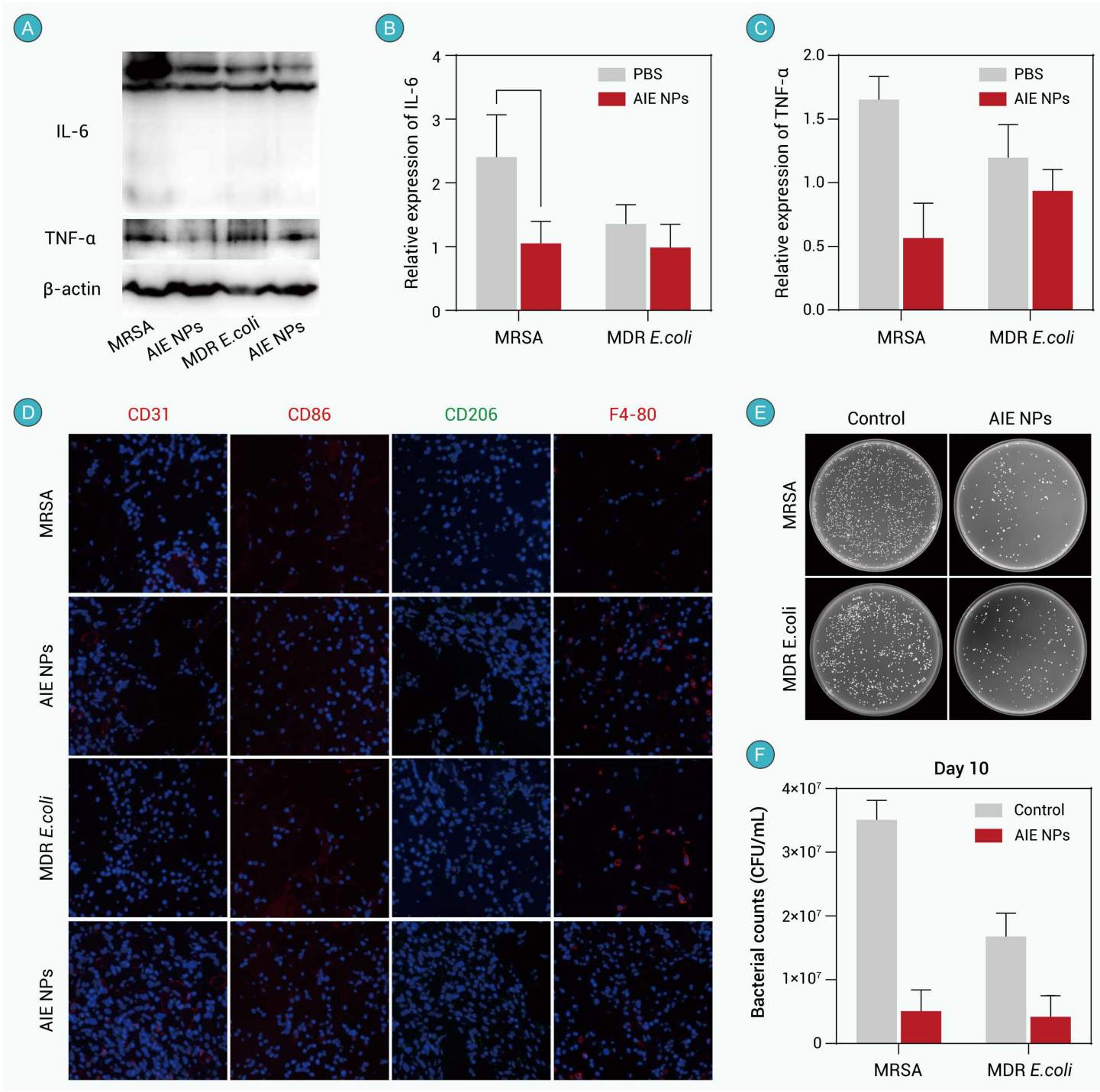

Figure 4. Evaluation of antibacterial efficacy and anti-inflammatory effects of AIE photothermal nanoparticles (A) Western blot results of infectious wound tissues after photothermal treatment. (B) and (C) Statistical result charts of the two inflammatory cytokines, IL-6 and TNF-α, in the wound tissue (data presented mean ± SD, n=3). $*p < 0.05$, $**p < 0.01$, $***p < 0.001$ (two-way ANOVA). (D) Immunofluorescence images of the treated wound tissue. (E) and (F) Bacterial plating results and quantity statistics of the tissue surrounding the wound after photothermal treatment (data presented mean ± SD, n=3).

NIR-II fluorescence emission for *in vivo* applications.

Compared with previously reported AIE-based photothermal or photodynamic antibacterial systems, the present platform emphasizes localized photothermal antibacterial activity combined with controlled nanoparticle fabrication via microfluidics, offering improved size uniformity and batch-to-batch reproducibility. These features are advantageous for biomedical applications requiring precise physicochemical control. However, it should be noted that current microfluidic fabrication strategies are inherently limited by relatively low throughput, which may restrict direct large-scale manufacturing for clinical use. To address this limitation, scalable strategies such as parallelization of microfluidic channels and scale-out device architectures have been proposed in recent studies and could be integrated into future designs.

CONCLUSION

Using a microfluidic chip, ultra-small photothermal nanoparticles were successfully prepared. The size of the nanoparticles can be precisely controlled by adjusting the flow rate, with the smallest nanoparticle size being around 18 nm. Not only do these microfluidic nanoparticles exhibit excellent water solubility and cellular biocompatibility, but they also demonstrate outstanding photothermal conversion capabilities, with the ability to heat up to 55°C, fully meeting the requirements of photothermal therapy applications.

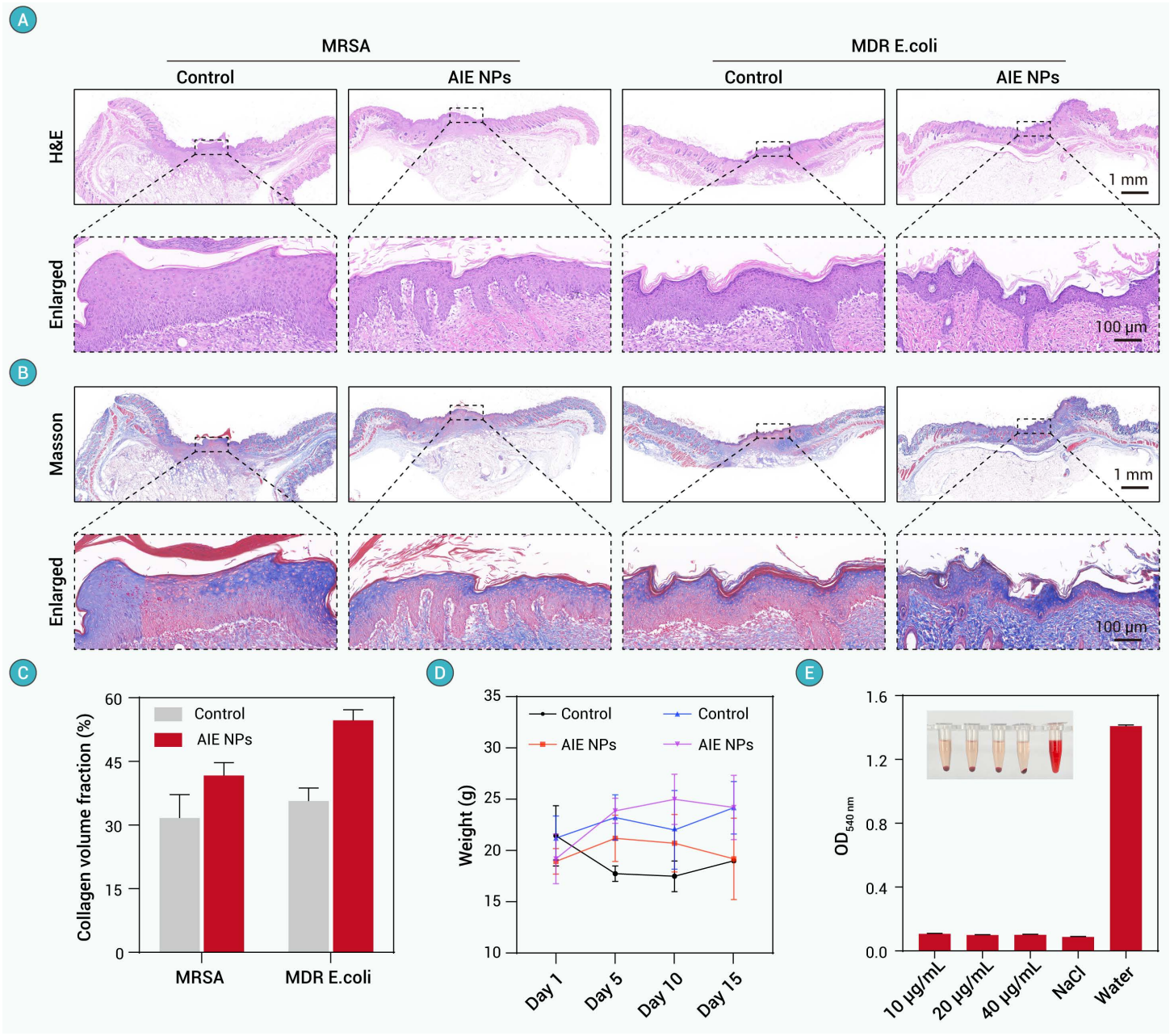

Figure 5. Evaluation of tissue regeneration and biosafety of AIE photothermal nanoparticles (A) HE staining results of wound tissue after photothermal treatment. (B) Masson staining results of wound tissue after photothermal treatment. (C) Statistical chart of collagen deposition in wound tissue. (D) Weight statistics of diabetic mice during the photothermal treatment process. (E) Results and statistics of the hemolysis experiment for the nanoparticles.

Using microfluidic nanoparticles combined with photothermal treatment, a broad-spectrum antibacterial effect can be achieved against both gram-negative and gram-positive bacteria, demonstrating excellent photothermal sterilization properties. In treating bacterial infections in chronic diabetic wounds, microfluidic nanoparticles exhibit a strong ability to prevent bacterial infections. A mere 10-minute laser irradiation can effectively kill antibiotic-resistant bacteria in the wound, significantly accelerating wound healing. Photothermal treatment with nanoparticles can significantly suppress the inflammatory response in wounds, promoting tissue regeneration and repair. This offers a new material and technological approach to expedite the healing of diabetic wounds and skin wound repair.

REFERENCES

1. Uberoi A., McCready-Vangi A. and Grice E. (2024). The wound microbiota: Microbial mechanisms of impaired wound healing and infection. *Nat. Rev. Microbiol.* **22**:507. DOI:10.1038/s41579-024-01035-z
2. Jeffcoate W. J., Bus S. A., Game F. L. et al. (2016). Reporting standards of studies and papers on the prevention and management of foot ulcers in diabetes: Required details and markers of good quality. *The Lancet* **4**:781. DOI:10.1016/s2213-8587(16)30012-2
3. Xin J., Gao L., Zhang W. et al. (2025). A thermogalvanic cell dressing for smart wound monitoring and accelerated healing. *Nat. Biomed. Eng.* **10**:80. DOI:10.1038/s41551-025-01440-6
4. Holt R. I. G., Cockram C. S., Ma R. C. W. et al. (2024). Diabetes and infection: Review of the epidemiology, mechanisms and principles of treatment. *Diabetologia* **67**:1168. DOI:10.1007/s00125-024-06102-x
5. Buch P. J., Chai Y. and Goluch E. D. (2019). Treating polymicrobial infections in chronic diabetic wounds. *Clin. Microbiol. Rev.* **32**:1128. DOI:10.1128/cmr.00091-18
6. Lafata J. E., Dobie E. A., Divine G. W. et al. (2009). Sustained hyperglycemia among patients with diabetes: What matters when action is needed. *Diabetes Care* **32**:1447. DOI:10.2337/dc08-2028
7. Chin J. S., Madden L., Chew S. Y. et al. (2019). Drug therapies and delivery mechanisms to treat perturbed skin wound healing. *Adv. Drug Delivery Rev.* **149**:2. DOI:10.1016/j.addr.2019.03.006
8. Zheng Z., Yang J., Zheng W. et al. (2025). Comprehensive management of diabetic ulceration: Strategies and perspectives. *J. Control. Release* **385**:114058. DOI:10.1016/j.jconrel.2025.114058

9. Xue Y., Zhou J., Lu Y. et al. (2025). Advancements in wound management: Microenvironment-sensitive bioactive dressings with on-demand regulations for diabetic wounds. *Engineering* **48**:234. DOI:10.1016/j.eng.2025.01.018
10. Wang X., Zhong B., Lou Z. et al. (2024). The advancement of intelligent dressings for monitoring chronic wound infections. *Chem. Eng. J.* **485**:149643. DOI:10.1016/j.cej.2024.149643
11. Manivasagan P., Thambi T., Joe A. et al. (2024). Progress in nanomaterial-based synergistic photothermal-enhanced chemodynamic therapy in combating bacterial infections. *Prog. Mater. Sci.* **144**:101292. DOI:10.1016/j.pmatsci.2024.101292
12. Xin H. L., Liu Y. Y., Xiao Y. N. et al. (2024). Design and nanoengineering of photoactive antimicrobials for bioapplications: from fundamentals to advanced strategies. *Adv. Funct. Mater.* **34**:2402607. DOI:10.1002/adfm.202402607
13. Li Y., Zhao Z., Zhang J. et al. (2018). A bifunctional aggregation-induced emission luminogen for monitoring and killing of multidrug-resistant bacteria. *Adv. Funct. Mater.* **28**:1804632. DOI:10.1002/adfm.202213353
14. Wang W., Gao Y., Zhang M. et al. (2023). Neutrophil-like biomimic AIE nanoparticles with high-efficiency inflammatory cytokine targeting enable precise photothermal therapy and alleviation of inflammation. *ACS Nano* **17**:7394. DOI:10.1021/acsnano.2c11762
15. Liu J., Wang Y. X., Gao W. J. et al. (2024). Development of D–A–D-Type NIR-II photothermal agents for synergistic eradication of multidrug-resistant bacteria and promoting diabetic wound healing. *Adv. Funct. Mater.* **35**:2411986. DOI:10.1002/adfm.202411986
16. Zhu L., Song G., Zhang W. et al. (2025). Aggregation induced emission luminogen bacteria hybrid bionic robot for multimodal phototheranostics and immunotherapy. *Nat. Commun.* **16**:2578. DOI:10.1038/s41467-025-57533-y
17. Wang W., Gao Y., Xu W. et al. (2024). The one-stop integrated nanoagent based on photothermal therapy for deep infection healing and inflammation inhibition. *Adv. Mater.* **36**:2307785. DOI:10.1002/adma.202307785
18. Yan D., Huang Y., Zhang J. et al. (2023). Adding flying wings: Butterfly-shaped NIR-II AIEgens with multiple molecular rotors for photothermal combating of bacterial biofilms. *J. Am. Chem. Soc.* **145**:25705. DOI:10.1021/jacs.3c09058
19. Qi J., Ou H. L., Liu Q. et al. (2021). Gathering brings strength: How organic aggregates boost disease phototheranostics. *Aggregate* **2**:95. DOI:10.1002/agt2.25
20. Kong X. W., Liang J., Lu M. et al. (2024). A NIR-II organic dendrimer with superb photothermal performance based on electron-donor iteration for photothermal immunotherapy. *Adv. Mater.* **36**:2409041. DOI:10.1002/adma.202409041
21. Xu C. and Pu K. (2021). Second Near-infrared photothermal materials for combinational nanotheranostics. *Chem. Soc. Rev.* **50**:1111. DOI:10.1039/d0cs00664e
22. Zhao Z., Zhang H. K., Tang B. Z. et al. (2020). Aggregation-induced emission: New vistas at aggregate level. *Angew. Chem. Int. Ed.* **59**:9888. DOI:10.1002/anie.201916729
23. Zhang R. Y., Shen P., Xiong Y. et al. (2024). Bright, photostable and long-circulating NIR-II nanoparticles for whole-process monitoring and evaluation of renal transplantation. *Nat. Sci. Rev.* **11**:nwad286. DOI:10.1093/nsr/nwad286
24. Duo Y. H., Han L., Yang Y. Q. et al. (2024). Aggregation-induced emission luminogen: role in biopsy for precision medicine. *Chem. Rev.* **124**:11242. DOI:10.1021/acs.chemrev.4c00244
25. Zhao Z., Chen C., Wu W. et al. (2019). Highly efficient photothermal nanoagent achieved by harvesting energy via excited-state intramolecular motion within nanoparticles. *Nat. Commun.* **10**:768. DOI:10.1038/s41467-019-08722-z
26. Gu H., Sun W., Du J. J. et al. (2024). Dual-acceptor engineering of donor-acceptor type molecules for all-round boosting anti-tumor phototherapy. *Smart Mol.* **2**:e20230014. DOI:10.1002/smo.20230014
27. Yan D. Y., Xie W., Zhang J. Y. et al. (2021). Donor/π-bridge manipulation for constructing a stable NIR-II aggregation-induced emission luminogen with balanced phototheranostic performance. *Angew. Chem. Int. Ed.* **60**:26769. DOI:10.1002/anie.202111767
28. Yan D. Y., Qin Y., Yan S. S. et al. (2023). Near-infrared emissive AIE nanoparticles for biomedical applications: From the perspective of different nanocarriers. *Particuology,* **74**:103. DOI:10.1016/j.partic.2022.06.001
29. Li B., Wang W., Zhao L. et al. (2024). Photothermal therapy of tuberculosis using targeting pre-activated macrophage membrane-coated nanoparticles. *Nat. Nanotechnol.* **19**:834. DOI:10.1038/s41565-024-01618-0
30. Middha E. and Liu B. (2020). Nanoparticles of organic electronic materials for biomedical applications. *ACS Nano* **14**:9228. DOI:10.1021/acsnano.0c02651
31. Meng Z. J., Ji X. H., Yin S. Y. et al. (2025). Preclinical studies on the photothermal therapy of NIR-II AIEgens: Across tumor types. *Small* **21**:e09080. DOI:10.1002/smll.202509080
32. Zhang Z., Kang M., Tan H. et al. (2022). The fast-growing field of photo-driven theranostics based on aggregation-induced emission. *Chem. Soc. Rev.* **51**:1983. DOI:10.1039/d1cs01138c
33. Kong L., He W., Gong J. et al. (2024). Photo-induced Bacillus subtilis-spore transformation for bowel disease therapy and therapeutic outcome visualization. *Aggregate* **5**:e597. DOI:10.1002/agt2.597
34. Chen D., Xiao T., Wang L. et al. (2024). A simple "spraying" fluorescence-guided surgery by AIE probes for liver tumor resection through configuration-induced cross-identification. *Aggregate,* **5**:e550. DOI:10.1002/agt2.550
35. Zhu Z. R., Liu S. C., Wu X. P. et al. (2025). An azo substituted quinoline-malononitrile enzyme-activable aggregation-induced emission nanoprobe for hypoxia imaging. *Smart Mol.* **3**:e20240028. DOI:10.1002/smo.20240028
36. Ding Q., Ding L., Xiang C. et al. (2025). pH-responsive AIE photosensitizers for enhanced antibacterial therapy. *Angew. Chem. Int. Ed.* **64**:e202506505. DOI:10.1002/anie.202506505
37. The C., Manghnani P., Boon G. et al. (2019). Bright aggregation-induced emission dots for dynamic tracking and grading of patient-derived xenografts in zebrafish. *Adv. Funct. Mater.* **29**:1901226. DOI:10.1002/adfm.201901226
38. Dong R. H., Liu Y., Mou L. et al. (2019). Microfluidics-based biomaterials and biodevices. *Adv. Mater.* **31**:1805033. DOI:10.1002/adma.201805033
39. Ma H., Kang Y. S., Xu W. Q. et al. (2025). An Immediate bacterial-responsive supramolecular thio-naphthalene diimide: A real-time NIR-II photothermal antibacterial. *Angew. Chem. Int. Ed.* **64**:e202505069. DOI:10.1002/anie.202505069

FUNDING AND ACKNOWLEDGMENTS

We are grateful for financial support from National Key Research and Development Program of China (2023YFB3810001 to Z.Z.), The Major Project of National Natural Science Foundation of China (22595401 to B.Z.T), National Natural Science Foundation of China (52333007 to B.Z.T), Guangdong Basic Research Center of Excellence for Aggregate Science, Key-Area Research and Development Program of Guangdong Province (2024B0101040001 to B.Z.T), the Key Research and Development Project of Yunnan Province (202303AC100010 to B.Z.T), the Science Technology Innovation Commission of Shenzhen Municipality (KQTD20210811090142053 to B.Z.T), the Young Taishan Scholars Program of Shandong Province (Grant No. tsqn202312246 to R.D), Shandong Provincial Natural Science Foundation (Grant No. ZR2024QE196 to R.D), Hong Kong scholar project (XJ2025018 to R.D). R. Dong, F. Ma, Z. Meng, and X. Ji contributed equally to this work. The funders had no role in study design, data collection and analysis, decision to publish, or preparation of the manuscript.

AUTHOR CONTRIBUTIONS

R. Dong, F. Ma, and Z. Zhao conceived the idea. F. Ma and H. Wen conducted molecular synthesis and spectroscopic measurements. R. Dong and Z. Meng conducted the setup of microfluidics chip and in vitro imaging. X. Ji conducted the cell viability. H. Wang supported molecular synthesis. R. Zhu, Z. Zhao, and B. Z. Tang supervised the project. R. Dong, F. Ma, and Z. Meng wrote the manuscript with inputs from all authors.

DECLARATION OF INTERESTS

The authors declare no competing interests.

ETHICAL STATEMENT AND PATIENT CONSENT

All animal procedures were applied per a protocol approved by the committee of the laboratory animal center at SUSTech (NO. JY202108030).

DATA AND CODE AVAILABILITY

All data supporting the findings of this study are available from the corresponding author upon reasonable request.

SUPPLEMENTAL INFORMATION

It can be found online at https://doi.org/10.59717/j.xinn-mater.2026.100216.